Chapter

Artificial Surfaces and Media for Electromagnetic Absorption and Interference Shielding

Pai-Yen Chen, Mohamed Farhat, Zhilu Ye, Muhammad Amin, Hakan Bagci and Danilo Erricolo

Abstract

The rapid advent of radio-frequency (RF) and microwave technologies and systems have given rise to serious electromagnetic pollution, interference and jamming for high-precision detection devices, and even threats to human health. To mitigate these negative impacts, electromagnetic interference (EMI) shielding materials and structures have been widely deployed to isolate sophisticated instruments or human settlements from potential EMI sources growing every day. We discuss recent advances in lightweight, low-profile electromagnetic absorbing media, such as metamaterials, metasurfaces, and nanomaterial-based solutions, which may provide a relatively easy solution for EMI shielding and suppressing unwanted RF and microwave noises. We present a general review of the recent progress on theories, designs, modeling techniques, fabrication, and performance comparison for these emerging EMI and electromagnetic compatibility (EMC) media.

Keywords: EMI, EMC, metamaterials, metasurfaces, perfect electromagnetic absorbers

1. Introduction

Electromagnetic absorbers have important applications in a plethora of applications, including but not limited to electromagnetic interferences and electromagnetic compatibility [1–5], stealth [6–9], camouflage [10], shielding [11–13], energy harvesting [14, 15], as well as antenna and optical measurements [2, 16–18]. Recently, the scientific interest has focused on EMC and EMI shielding that studies how to suppress noise or interference in various electronic appliances and radiative damage to humans caused by unintended EM signals. In these applications, electromagnetic absorbers play an essential role. As one of the representative examples, a high-performance and cost-effective anechoic chamber, which can provide a zero-reflection environment mimicking free space, is of paramount importance for EMC test, antenna, and scattering measurements, among many other applications. As illustrated in **Figure 1(a)**, in an anechoic chamber, the entire inner surfaces (walls, ceiling, and floor) are properly covered with absorbers to absorb waves propagating toward them and thus eliminate multipath interferences. Hence, a simple and well-defined propagation channel can be obtained between the transmitting source and

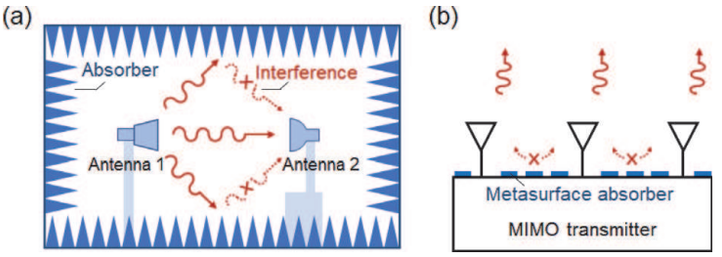

Figure 1.
Examples of practical applications of electromagnetic absorbers in EMC/EMI: (a) an anechoic chamber and (b) a high-isolation MIMO antenna system.

receiving antennas or a scattering object for radar cross-section (RCS) measurements. Nearly perfect absorption, realized with an ultrathin, lightweight, and low-cost manner, makes the artificial surfaces and media (i.e., metamaterials and metasurfaces) advantageous over the conventional electromagnetic absorbers made of natural materials. Ever since the first perfect metamaterial absorber was proposed by Landy *et al.* [19], numerous designs have been proposed for metamaterial or metasurface absorbers over a wide range of frequencies [20–25] and even with multiband operation [1, 26–28].

The applications include RCS reduction and stealth [29], EMI shielding [12, 13], sensing [30–33], terahertz imaging [34–36], energy harvesting, etc. A representative modern application of metamaterial absorbers may be the enhanced isolation in the multiple-input-multiple-output (MIMO) antenna system [37, 38], as depicted in **Figure 1(b)**. With the growing demand for miniaturization of telecommunication devices, reducing the mutual coupling or cross-talk among the antenna elements has been a challenging task in MIMO systems. A specifically designed metamaterial absorber mostly consisting of periodic resonators can help improve the isolation among antenna elements and further enhance the efficiency of a MIMO system since it can significantly absorb the unwanted interferences among antennas.

The impedance of a material is defined as $\sqrt{\mu_r\mu_0/\varepsilon_r\varepsilon_0}$, with ε_r, ε_0 (μ_r, μ_0) denoting the relative permittivity, permittivity of free space (the relative permeability, permeability of free space), respectively [39]. At microwave frequencies and even at the terahertz (THz), most of the naturally occurring materials (used, for instance, in microelectronics) exhibit very low to nonexistent magnetic resonances and thus $\mu_r \approx 1$ [40]. On the other hand, the relative permittivity can attain extremely high values, e.g., in conductors such as noble metals or graphene (in the THz regime). So, the impedance is generally much smaller than that of the surrounding ($\eta/\eta_0 \approx 1/\sqrt{\varepsilon_r} \ll 1$) [41]. This huge mismatch can cause a strong reflection of the electromagnetic signal and perturb the operation of the electrical equipment. In this context, electromagnetic compatibility is an important and active field of research that endeavors to limit undesired and unintentional scattering of microwave and THz waves to avoid, for example, unwanted behavior such as electromagnetic interference [42]. The impedance matching with the free space is hence a necessary condition to reduce much of the reflection of the incident wave. One avenue consists of a large effective relative permeability μ_r by tailoring custom RF, microwave, and THz metamaterials [43, 44]. These are artificial materials structured at the nano- or micro-scale and gained tremendous attention over the past two decades thanks to their exotic dynamic properties, generally not found in nature, such as negative optical refraction [45, 46], and electromagnetic cloaking [47, 48]. The collective oscillations of free electrons in metals, termed localized or delocalized surface plasmon polaritons (SPPs) [49], are at the origin of these unique properties, allowing a multitude of intriguing applications such as biosensors [50], optical filters [51], photodetectors [52], and nanolasers [53] to name a few.

The metallic nanostructures based on localized SPP resonance generally create strongly enhanced electromagnetic fields. The electric field confined in the junctions of metal particles, so-called electrical hot spots [49], allows for a significant improvement in emission processes and non-linearities [54], which are mediated by the electrical polarization of molecules. In particular, the magnetic activity at optical frequencies is much lower than its electrical equivalent due to the extremely low magnetic response of natural materials [40]. Accordingly, magnetic hot spots are highly desirable for enhancing the magnetic response. Many structures have been specifically designed to provide magnetic hot spots, such as diabolo antennas [55] and two parallel metal plates [56]. However, achieving simultaneous electric and magnetic hot spots in the same spatial position is rather difficult. In addition, quality factor and mode volume are critical parameters in local field enhancement engineering.

In the same vein, although the intrinsic optical loss of metals is a major limitation in the performance of these devices, it is beneficial in improving light absorption. In 2008, Landy *et al.* first proposed a perfect metamaterial absorber with near-perfect absorption by simultaneously exciting electric and magnetic resonances to achieve impedance matching with free space [19]. Soon after, important absorber designs based on different physical mechanisms have been demonstrated theoretically and experimentally in a broad spectral range, which can be classified into two categories: narrowband absorbers [57, 58] and broadband absorbers [59, 60] in terms of their absorption bandwidth. While broadband absorbers are typically used in thermophotovoltaic systems [61], perfect narrowband absorbers may be used for absorption filters [36], tailoring thermal radiation [62], and sensing [30, 32]. For the important sensing and detection applications, the experimentally performed refractive index (RI) sensor based on infrared coherent perfect absorber (CPA) shows that a narrow bandwidth and a large modulation depth are required for better performance [32, 33]. The three-layered configuration of metal–insulator–metal (MIM) employed was widely applied to the following SPP absorbers, where a thin dielectric spacer is sandwiched to allow for strong plasmonic coupling between the top resonators and the bottom metallic reflector as discussed in depth in [22, 59]. This class of CPA designs may also be intuitively treated as a single input transmission line (TL) coupled to a plasmonic resonator, where the thickness of the insulating spacer affects the radiative damping rates as well as the resonance frequency bandwidth.

2. Generalized theory for perfect electromagnetic absorbers

In this section, we will discuss the basic principles of extremely thin electromagnetic absorbers composed of an infinite two-dimensional array of electric dipoles, magnetic dipoles, or both. According to the optical theorem, when the scatterer interacts with the incident fields, the power depleted from the incident fields is the sum of the absorbed and scattered powers, i.e., $P_{ext} = P_a + P_s$. This power balance is fundamentally restricted by the energy conservation enforced by causality. The time-averaged absorbed power is the surface integral of the inward flowing flux of the Poynting vector over the surface surrounding the scatterer [63].

$$P_a = -\frac{1}{2}\,\mathrm{Re}\left[\oiint(\mathbf{E}_{inc} + \mathbf{E}_s) \times (\mathbf{H}_{inc} + \mathbf{H}_s)^* \cdot \hat{n}\, ds\right], \tag{1}$$

where $\{\mathbf{E}_{inc}, \mathbf{H}_{inc}\}$ and $\{\mathbf{E}_s, \mathbf{H}_s\}$ are the incident and scattered fields, respectively. Similarly, the time-averaged scattered power representing the re-radiated power from the scatterer is the surface integral of the outward flux of the Poynting vector of scattered fields,

$$P_s = \frac{1}{2}\,\mathrm{Re}\left[\oiint \mathbf{E}_s \times \mathbf{H}_s^* \cdot \hat{n}\, ds\right]. \tag{2}$$

Finally, the total incident power flowing through the surface S is zero

$$P_{inc} = \frac{1}{2}\,\mathrm{Re}\left[\oiint \mathbf{E}_{inc} \times \mathbf{H}_{inc}^* \cdot \hat{n}\, ds\right] \equiv 0. \tag{3}$$

From Eqs. (1)-(3), the total extracted power (power extinction) is given by the cross-terms

$$P_{ext} = -\frac{1}{2}\,\mathrm{Re}\left[\oiint \left(\mathbf{E}_i \times \mathbf{H}_s^* + \mathbf{E}_s \times \mathbf{H}_i^*\right) \cdot \hat{n}\, ds\right]. \tag{4}$$

The forward scattering sum rule is valid for any arbitrary absorbers, for which the scattered power P_s is the sum of the backward scattered (reflected) power $P_r = |R|^2 P_{inc}$ and the forward scattered power (i.e., the difference between the transmitted and incident fields) $P_f = |1 - T|^2 P_{inc}$ where$R$ and T are reflection and transmission coefficients of the compact planar absorber, respectively. The total scattered power P_s can be expressed as

$$P_s = P_r + P_f = \left(|R|^2 + |1 - T|^2\right) P_{inc}. \tag{5}$$

The absorbed power P_a is the difference between the incident power and the sum of reflected and transmitted power $P_r + P_t$, given by

$$P_a = P_{inc} - P_r - P_t = \left(1 - |R|^2 - |T|^2\right) P_{inc}. \tag{6}$$

Assuming that there are no grating sidelobes, the power extinction -P_{ext} can be written as

$$P_{ext} = P_a + P_s = 2\,\mathrm{Re}\,[1 - T] P_{inc}. \tag{7}$$

This can be seen as the optical theorem for infinite two-dimensional (2D) planar structures, such as metascreens or an ultrathin absorptive film. We know from Eqs. (5)-(7) that when the forward scattered power represents the total scattered power, i.e., no backward scattered (reflected) waves, the total absorption of the incident radiation can be achieved. In this case, the scattered power equals the absorbed power, $P_s = P_f = P_a$, which is somehow similar to the conjugated matching concept in the equivalent Thevenin or Norton circuit. The 100% absorption occurs only for an asymmetric system, such as a metal-back thin absorptive slab or a surface that combines both electric and magnetic dipoles [64]. For instance, electric and magnetic dipole arrays at the metascreen would radiate symmetric and anti-symmetric electric fields on either side of the metascreen. The anti-symmetry introduced by magnetic dipoles enables the complete cancelation of incident fields in the forward direction while generating no backward propagating wave, thereby achieving a perfect absorption [39]. Likewise, a metal-backed electric or magnetic dipole array, such as linear dipole or patch antenna array, also exhibits the asymmetry necessary for making a perfect absorber, which will be discussed in the following.

Consider an infinite 2D electric dipole array, separated from a PEC ground plane by a distance d; this induces an electric current sheet parallel to the ground PEC plane, as shown in **Figure 2** (a). We assume that the array period is smaller than the

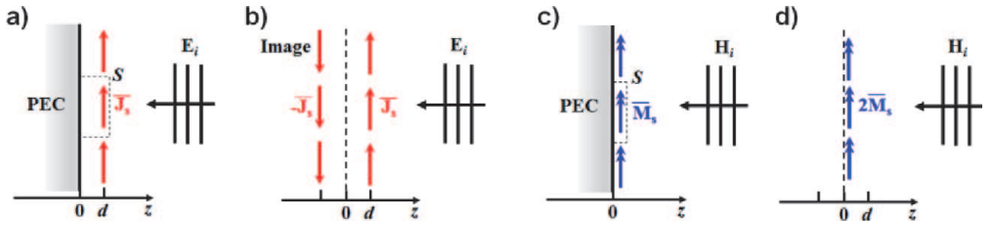

Figure 2.
(a) Electric and (c) magnetic sheet currents over a PEC surface and the corresponding images (b) and (d), respectively.

wavelength of the incident wave, and the array is excited by an x -polarized normally incident plane wave from the positive z-direction: $E_{inc} = \hat{\boldsymbol{x}} E_0 e^{jkz}$, where k is the wavenumber of the uniform background medium. For brevity, we consider an isotropic periodic grid that can be conveniently modeled by a scalar surface impedance Z_s, relating the surface-averaged electric field $\mathbf{E}_{\text{tot}} = \mathbf{E}_{\text{inc}} + \mathbf{E}_{\text{s}}$ in the array plane and the average electric surface current density of complex amplitude $\mathbf{J}_{\text{s}} = \hat{\boldsymbol{x}} J_{\text{s}} = \hat{\boldsymbol{x}} J_{\text{s0}} e^{i\varphi}$ (which is expressed in terms of the averaged tangential magnetic fields on the two sides of the array)

$$\mathbf{J}_{\text{s}} = \frac{j\omega\ \mathbf{p}}{S} = \hat{\boldsymbol{z}} \times (\mathbf{H}^{+} - \mathbf{H}^{-}) = \mathbf{E}_{\text{tot}} / Z_s, \tag{8}$$

where $\mathbf{p}$ is the electric dipole moment generated by the resonant meta-atoms, $\mathbf{E}_{\text{s}}$ is the scattered fields generated by the average electric surface current density $\mathbf{J}_{\text{s}}$ and S is the area of a unit-cell. This scattering problem can be solved using the image theory, which removes the ground plane and places an image source of $-\mathbf{J}_s$ at $z = -d$. With the principle of superposition, the total fields for $z > 0$ can be found by combining the fields from the two sources individually. Hence, the scattered electric and magnetic fields can be written as

$$\begin{aligned} E_s &= \begin{cases} -\hat{\boldsymbol{x}} j J_{\text{s}} \eta e^{-jkd} \sin kz + E_0 e^{-jkz}, & 0 < z < d \\ -\hat{\boldsymbol{x}} j J_{\text{s}} \eta \sin kd e^{-jkz} + E_0 e^{-jkz}, & z > d \end{cases}; \\ H_s &= \begin{cases} \hat{\boldsymbol{y}} j J_{\text{s}} e^{-jkd} \cos kz - \dfrac{E_0}{\eta} e^{jkz}, & 0 < z < d \\ -\hat{\boldsymbol{y}} j J_{\text{s}} \sin kd e^{-jkz} + \dfrac{E_0}{\eta} e^{jkz}, & z > d, \end{cases}; \end{aligned} \tag{9}$$

where η is the intrinsic impedance of the background medium. The second terms in Eq. (9) are contributed by the reflection (backward scattering) from the conducting ground plane, whereas the first terms in Eq. (9) are produced by the induced surface current. Below the ground plane ($z > 0$), the scattering fields $\mathbf{E}_s = -\mathbf{E}_{inc}$ are always valid, regardless of the scattering environment above the ground plane. As known from Eqs. (1) and (2), the time-averaged scattered and absorbed power can be obtained from the surface integral of the inward flowing flux of the Poynting vector of the total field through the surface S enclosing a single unit-cell

$$\begin{aligned} P_s &= \frac{1}{2} \text{Re} \left[\oiint \mathbf{E}_s \times \mathbf{H}_s^{*} \cdot \hat{n}\, ds \right] \\ &= \frac{E_0^2}{\eta_0} + \frac{1}{2} J_{s0}^2 \eta_0 \sin^2 (k_0 d) - E_0 J_{\text{s0}} \sin (k_0 d) \sin (\varphi), \end{aligned} \tag{10}$$

$$P_a = -\frac{1}{2}\,\mathrm{Re}\left[\oiint(\mathbf{E}_{inc}+\mathbf{E}_s)\times(\mathbf{H}_{inc}+\mathbf{H}_s)^*\cdot\hat{n}\,ds\right] = J_{s0}E_0\sin(k_0d)\sin(\varphi)-\frac{1}{2}J_{s0}^2\eta_0\sin^2(k_0d). \tag{11}$$

For an arbitrary value d, the perfect absorption can be achieved when the surface electric current is tailored to be

$$J_s = \frac{E_0}{\eta\sin(kd)}\mathrm{e}^{j(\pi/2)}, \tag{12}$$

or from Eqs. (8), (9), and (12), we obtain the optimum (lossy and capacitive) surface impedance $Z_{s,opt}$ that renders the maximum absorbed power and $P_{abs} = P_{sca}$

$$Z_{s,opt} = \frac{\eta}{2}\left[2\sin^2(kd) - j\sin(2kd)\right]. \tag{13}$$

When the distance between the array plane and the ground plane $d = \lambda/4$, the optimum electric surface impedance $Z_{s,opt} = \eta$; such a result is consistent with the setting of the Salisbury screen absorber [65]. From Eq. (13), we find that a complex surface impedance is required to miniaturize an absorber with $kd \to 0$. Intuitively, a capacitive lossy surface with$\mathrm{Im}\left[Z_{s,opt}\right] = -j\eta\sin(2k_0d)/2 \simeq -j\omega\mu d$ should be exploited to compensate for the shunt inductance resulting from the grounded dielectric substrate that exhibits an input impedance $\mathrm{Z}_{in} = j\eta\tan(kd) \approx j\omega\mu d$. An equivalent TL model sketched in **Figure 3** may be a straightforward way to describe the reflection and absorption properties of the grid array. For a plane wave normally incident on the structure, the zero reflection condition (i.e., total absorption) can be obtained as $\mathrm{Z}_{in}^{-1} + \mathrm{Z}_s^{-1} = \eta^{-1}$, leading to the same results of Eq. (13).

In the following, we briefly discuss how to design and synthesize the grid array that provides the required surface impedance. It is instructive to study a metamaterial surface or metasurface formed by a 2D array of meta-atoms excited by an external electric field $\mathbf{E}_{\mathrm{ext}}$ with the TE polarization (**Figure 2a**). The collective behavior of electric dipole moments induced in electric meta-atoms will result in a homogenous sheet current. The total averaged polarization related to the local field is responsible for the$\alpha_{\mathrm{e,xx}}$ component of the electric polarizability tensor $\boldsymbol{\alpha}_{\mathrm{e}}$. Considering the full coupling among the whole array of interacting electric dipoles, the dipole moment induced on the nanoparticle is given by [35, 66, 67].

$$p_{\mathrm{NxNy}} = \alpha_{\mathrm{xx}}E_{\mathrm{loc}} = \alpha_{\mathrm{e,xx}}^{-1}\left[E_{\mathrm{ext}} + \varepsilon^{-1}\sum_{(\mathrm{N_x},\mathrm{N_y})\neq(\mathrm{N'_x},\mathrm{N'_y})} G\left(r_{\mathrm{N_xN_y}} - r_{\mathrm{N'_x,N'_y}}\right)\cdot p_{\mathrm{N'_x,N'_y}}\right] \tag{14}$$

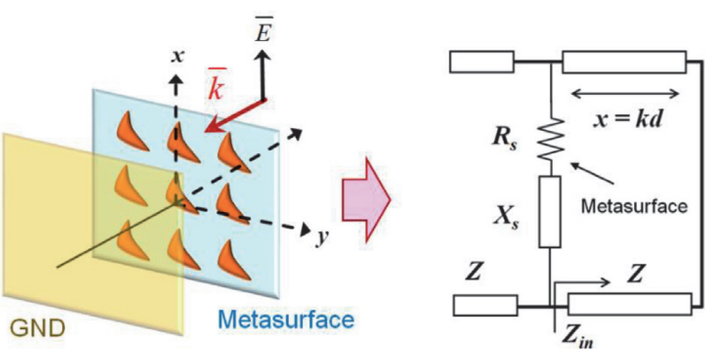

Figure 3.
Equivalent transmission line model of an ultrathin metasurface-based absorber.

where N_x and N_y are positive or negative integers, which relate the position of local dipoles and periods d_x and d_y by $x = N_x d_x$ and $y = N_y d_y$, $r_{N_x N_y}$ is the position of the dipole p^{NxNy}, and $G\left(r_{N_x N_y}, r_{N'_x N'_y}\right) = \left(\nabla\nabla + k^2\bar{\bar{I}}\right)\frac{e^{-jk\left|r_{N_x N_y} - r_{N'_x N'_y}\right|}}{4\pi\left|r_{N_x N_y} - r_{N'_x N'_y}\right|}$ is the dyadic Green's function in a homogeneous and isotropic medium. After some algebraic manipulations, we may write (14) as:

$$p_{00} = p_{00}\hat{\boldsymbol{x}} = \frac{1}{\alpha_{e,xx}^{-1} - \beta}E_{ext} \tag{15}$$

where $\beta = \sum_{(N_x, N_y)\neq(0,0)} G\left(r_{N_x N_y}, r_{N'_x N'_y}\right)\hat{\boldsymbol{x}}\hat{\boldsymbol{x}}$ is the interaction constant that relates the fields induced by the infinite array of electric dipoles around the unit cell under consideration to the local field at the origin. The averaged surface current density on the metasurface can be expressed as:

$$J_s = J_s\hat{\boldsymbol{x}} = \frac{j\omega p_{00}}{S} = \frac{j\omega E_{ext}}{S\left(\alpha_{e,xx}^{-1} - \beta\right)}\hat{\boldsymbol{x}}, \tag{16}$$

where the area of the metasurface lattice S = $d_x d_y$. This is an accurate description of the array's electromagnetic properties, as long as the periods are small enough to ensure that only one Floquet harmonic could exist. The average surface impedance of metasurface, as the ratio of the local electric field to the surface current density, can be expressed as

$$Z_s = \frac{E_{ext}}{J_s} - \frac{\eta}{2} = \frac{S}{j\omega}\left(\alpha_{e,xx}^{-1} - \beta\right) - \frac{\eta}{2} \tag{17}$$

Under the lossless and low frequency condition, the polarizability is approximately given by $\alpha_{e,xx}^{-1} \simeq \alpha_{e0,xx}^{-1} + jk^3/(6\pi\varepsilon)$, where $\alpha_{e0,xx}$ is the static polarizability. Eq. (17) may be further manipulated by considering the physical requirements on the imaginary parts of β associated with the power balance [68].

$$Im[\beta] = \frac{k^3}{6\pi\varepsilon} - \frac{\eta\omega}{2S} \tag{18}$$

So, Eq. (17) can be further reduced to

$$Z_s = \frac{S}{j\omega}\left(\alpha_{e0,xx}^{-1} - \mathrm{Re}\,[\beta]\right) - \frac{\eta}{2}. \tag{19}$$

For a subwavelength lattice, i.e., $kd_x, kd_y \ll 1$, the real part of quasi-static approximate interaction coefficient can be written as [69].

$$\mathrm{Re}\,[\beta] = \frac{1}{\varepsilon\pi d_x^3}\sum_{m=1}^{\infty}\frac{1}{m^2} - \frac{8\pi}{\varepsilon d_x^3}\sum_{m=1}^{\infty}\sum_{n=1}^{\infty} m^2 K_0\left(mn2\pi\frac{d_y}{d_x}\right), \tag{20}$$

where $K_0(\cdot)$ is the modified Bessel function of the second kind (or Macdonald function [70]). For the square lattice $\left(d_x = d_y \ll \lambda_0\right)$, the Eq. (20) can have a compact form

$$\mathrm{Re}\,[\beta] \simeq \frac{1}{\varepsilon \mathrm{d}_\mathrm{x}^3}\left(-\frac{\psi_2(1)}{2\pi} - 8\pi \mathrm{K}_0(2\pi)\right) \simeq \frac{0.3596}{\varepsilon \mathrm{d}_\mathrm{x}^3}, \tag{21}$$

where ψ_n is the polygamma function [71]. Eq. (21) agrees with the low-frequency interact coefficient in Ref. [72]:

$$\begin{aligned}\beta &\simeq -\mathrm{j}\omega\frac{\eta}{4\mathrm{d}_\mathrm{x}^2}\left(1-\frac{1}{\mathrm{jkR}_0}\right)\mathrm{e}^{-\mathrm{jkR}_0} + \mathrm{Im}\left[\alpha_{\mathrm{e,xx}}^{-1}\right] \\ &\simeq \frac{0.3596}{\varepsilon \mathrm{d}_\mathrm{x}^3} - \mathrm{j}\left(\frac{\eta\omega}{2\mathrm{d}_\mathrm{x}^2} + \frac{\mathrm{k}^3}{6\pi\varepsilon}\right).\end{aligned} \tag{22}$$

where $\mathrm{R}_0 \simeq \mathrm{d}_\mathrm{x}/1.438$ and $\mathrm{Re}\,[\beta] \simeq 0.3596/\left(\varepsilon \mathrm{d}_\mathrm{x}^3\right)$. From Eqs. (13) and (19), we find that the maximum absorption is reached when the following conditions are satisfied:

$$\mathrm{Re}\left[\alpha_{e0,\mathrm{xx}}^{-1}\right] - \mathrm{Re}\,[\beta] = \frac{\omega\eta}{2S}\sin(2kd); \tag{23}$$

$$\mathrm{Im}\left[\alpha_{e0,\mathrm{xx}}^{-1}\right] = \frac{\omega\eta}{S}\left(1-\frac{\cos(2kd)}{2}\right). \tag{24}$$

This can be achieved by tailoring the size, shape, and material property (i.e., dispersion of the complex permittivity) of the elementary inclusion (i.e., meta-atom) in the metasurface unit-cell. For a Salisbury-type absorber with $d = \lambda/4$, Eqs. (23) and (24) becomes:

$$\mathrm{Re}\left[\alpha_{e0,\mathrm{xx}}^{-1}\right] \approx \mathrm{Re}\,[\beta], \tag{25}$$

$$\mathrm{Im}\left[\alpha_{e0,\mathrm{xx}}^{-1}\right] \approx \frac{\omega\eta}{S} = \frac{k}{\varepsilon S}. \tag{26}$$

The first condition implies an individual scatterer is at its self-resonance, which considers the cancelation of a general sense, the maximum absorption cross-section of each inclusion in densely packed arrays $\sigma_\mathrm{sca} = S$ is smaller than that of the same inclusion in free reactive coupling between neighboring scatters. In contrast, the second condition means that the absorption in the array is maximized; such occurs when the absorbed power is equal to the re-radiated power, i.e., $P_{abs} = P_{sca} = |E_{inc}|^2/2\eta = P_{in}$. We note that the maximum absorbed power for each lattice is $P_{abs,cell} = SP_{in}$, therefore, in space under the same illumination $\sigma_\mathrm{sca} = 3\lambda^2/8\pi$. It is interesting to note that inclusion in the grid can absorb as much as it is in free space when the unit cell size is: $k^2S = 3\pi/2$. In the low-frequency region, the polarizability of a generalized inclusion is $\boldsymbol{\alpha}_e^{-1} = \boldsymbol{\alpha}_{e0}^{-1} + \frac{k^3}{6\pi\varepsilon}\mathbf{I}$. The static polarizability of a meta-atom as a function of geometry, frequency, and material property can be analytically derived or numerically retrieved. For example, the static polarizability of a spherical particle is: $\boldsymbol{\alpha}_{e0} = 4\pi a^3\varepsilon_0\frac{\boldsymbol{\varepsilon}_D-\varepsilon}{\boldsymbol{\varepsilon}_D+2\varepsilon}$ [39], where a and $\boldsymbol{\varepsilon}_D$ are the radius and permittivity tensor of the spherical scatterer. For a 2D structure with negligible thickness, such as a square patch or circular disk, the static polarizability is in the form of $\boldsymbol{\alpha}_{e0} = \alpha_{e,xx}\hat{\boldsymbol{x}}\hat{\boldsymbol{x}} + \alpha_{e,yy}\hat{\boldsymbol{y}}\hat{\boldsymbol{y}}$. For example, for a conducting circular disk $\alpha_{e0,xx} = \alpha_{e0,yy} = 16\pi a^3/3\varepsilon$ where a is its radius. In the extreme case, the polarizability of a 1D conducting rod with a deeply subwavelength radius a and height h, aligned parallel to the electric field of the incident wave, has only the $\alpha_{e,xx}$ component [39]. For

modern meta-atom designs such as electric or magnetic split-ring resonators [73–77], the resonant electric/magnetic polarizability can be fitted to a generalized Lorentzian dispersion model

$$\alpha_{e/m}(\omega) = \frac{A\omega^2}{\omega_0^2 - \omega^2 + j\omega\Gamma}, \tag{27}$$

where ω_0 is the resonant frequency of electric/magnetic polarizability,Γ is the damping factor, and A is the amplitude.

Figures 4 and **5** show metasurface absorbers based on 2D arrays of plasmonic disks [78] and electric ring resonators [79], respectively. It is clearly seen that the ultrathin and low-profile metasurface absorbers can significantly absorb the incident wave in the frequency band of interest. We note that these electric resonant inclusions can be equivalent to a 2D array of electric dipoles discussed above.

It is also possible to exploit a metasurface constituted by magnetic or magneto-electric meta-atoms [9, 19, 22, 23] to build a perfect electromagnetic absorber. For example, **Figure 2(c)** and **(d)** consider a magnetic dipole array over a ground plane and the image. When a plane wave normally incident on the structure, the magnetic current density is induced: $\mathbf{M}_s = j\omega\mathbf{m}_{00}/S$. In a generalized scenario, the metasurface is excited by normally incident plane wave with fields ($\mathbf{E}_{ext}$, $\mathbf{H}_{ext}$), and an individual meta-atoms is excited by the local field ($\mathbf{E}_{loc}$, $\mathbf{H}_{loc}$):

$$\begin{aligned} \mathbf{p}_{00} &= \boldsymbol{\alpha}_e \mathbf{E}_{loc} + \boldsymbol{\alpha}_{em} \mathbf{E}_{loc}; \\ \mathbf{m}_{00} &= \boldsymbol{\alpha}_{me} \mathbf{E}_{loc} + \boldsymbol{\alpha}_m \mathbf{E}_{loc}, \end{aligned} \tag{28}$$

and

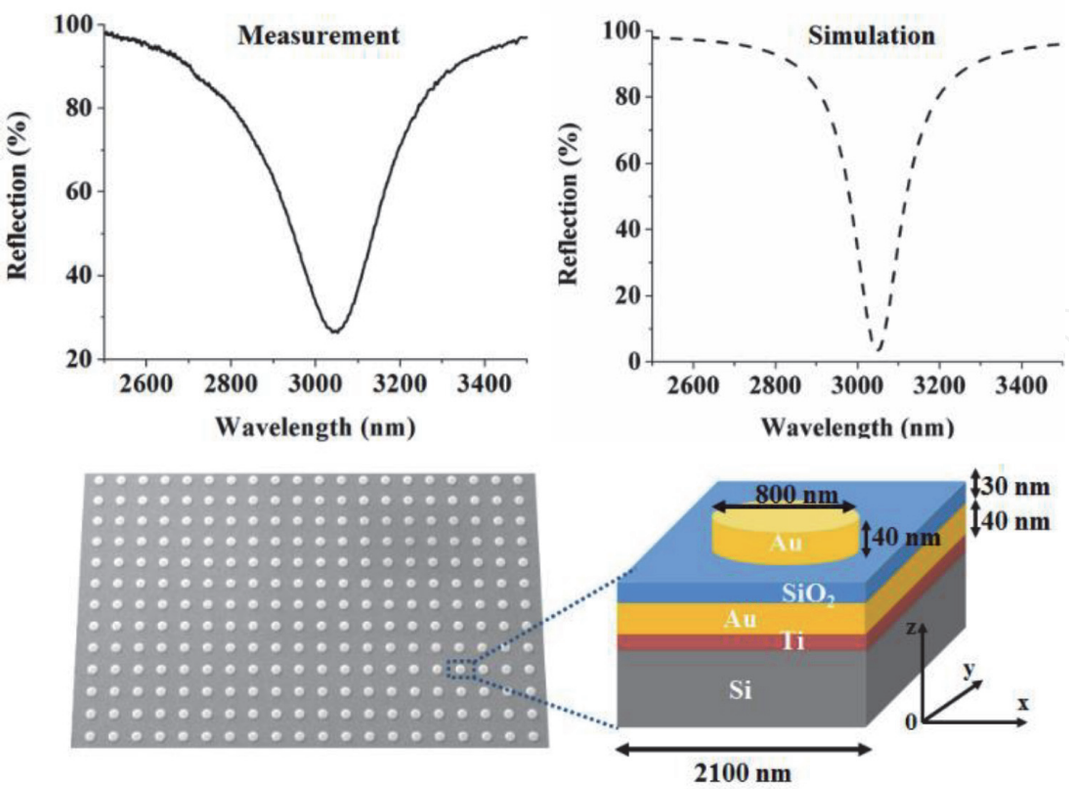

Figure 4.
Comparison between measurement and simulation. Above: Reflection spectra of the metamaterial absorber consisting of periodic arrays of Au cylinders/disks deposited on a stack of SiO_2/Au/Ti/Si layers measured by FTIR spectrometer and calculated by FDTD simulation. Bottom: SEM image of the absorber and a relevant unit cell needed for simulation.

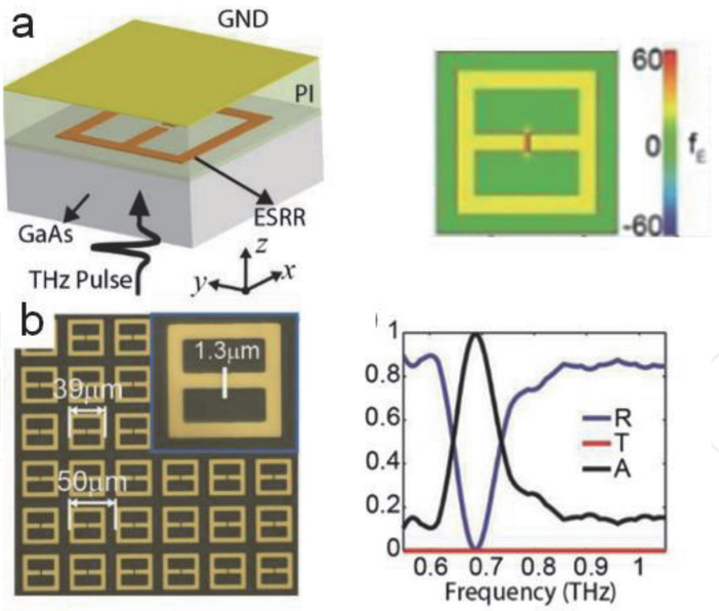

Figure 5.
(a) Terahertz metasurface absorber based on electric resonant inclusions, which displays a strong electric field localization in the capacitive gap region. (b) Transmission, reflection, and absorption against frequency for the metasurface in (a).

$$\begin{aligned}\mathbf{E}_{loc} &= \mathbf{E}_{ext} + \mathbf{p}_{00} \cdot \boldsymbol{\beta};\\ \mathbf{H}_{loc} &= \mathbf{H}_{ext} + \mathbf{m}_{00} \cdot \boldsymbol{\beta}',\end{aligned} \tag{29}$$

where $\boldsymbol{\alpha}$ is the dyadic polarizability and the interaction coefficient are

$$\boldsymbol{\beta} = \beta\mathbf{I} + j\left(\frac{\eta\omega}{2S} + \frac{\mathrm{k}^3}{6\pi\varepsilon}\right)\mathbf{I} \quad \text{and} \quad \boldsymbol{\beta}' = \frac{\boldsymbol{\beta}}{\eta^2}. \tag{30}$$

The total averaged fields on the metasurface can be expressed as

$$\begin{pmatrix}\mathbf{E}_{tot}\\ \mathbf{H}_{tot}\end{pmatrix} = \begin{pmatrix}\mathbf{Z}_e & \mathbf{Z}_{em}\\ \mathbf{Z}_{me} & \mathbf{Z}_m\end{pmatrix} \cdot \begin{pmatrix}\mathbf{J}\\ \mathbf{M}\end{pmatrix}, \tag{31}$$

where the surface impedances are given by

$$\begin{aligned}\mathbf{Z}_e &= -j\frac{S}{\omega}\left[\left(\boldsymbol{\alpha}_e - \boldsymbol{\alpha}_{em}\cdot\boldsymbol{\alpha}_{mm}^{-1}\cdot\boldsymbol{\alpha}_{me}\right)^{-1} - \boldsymbol{\beta}_e - j\frac{\eta\omega}{2S}\mathbf{I}\right];\\ \mathbf{Z}_m &= -j\frac{S}{\omega}\left[\left(\boldsymbol{\alpha}_m - \boldsymbol{\alpha}_{me}\cdot\boldsymbol{\alpha}_{ee}^{-1}\cdot\boldsymbol{\alpha}_{em}\right)^{-1} - \boldsymbol{\beta}_m - j\frac{\omega}{2\eta S}\mathbf{I}\right];\\ \mathbf{Z}_e &= -j\frac{S}{\omega}\left[\left(\boldsymbol{\alpha}_e - \boldsymbol{\alpha}_{em}\cdot\boldsymbol{\alpha}_{mm}^{-1}\cdot\boldsymbol{\alpha}_{me}\right)^{-1} - \boldsymbol{\alpha}_{em}\cdot\boldsymbol{\alpha}_{mm}^{-1}\right];\\ \mathbf{Z}_e &= -j\frac{S}{\omega}\left[\left(\boldsymbol{\alpha}_m - \boldsymbol{\alpha}_{me}\cdot\boldsymbol{\alpha}_{ee}^{-1}\cdot\boldsymbol{\alpha}_{em}\right)^{-1} - \boldsymbol{\alpha}_{me}\cdot\boldsymbol{\alpha}_{ee}^{-1}\right].\end{aligned} \tag{32}$$

If the reader is interested in learning details about anisotropic magnetoelectric metasurfaces, please see Refs. [80–82].

Figure 6 shows an ultrathin electromagnetic absorber based on resonant magnetic structures. Under the excitation of a plane wave, a magnetic dipole array can be induced, and at resonance, the incident power can be absorbed, analogous to the

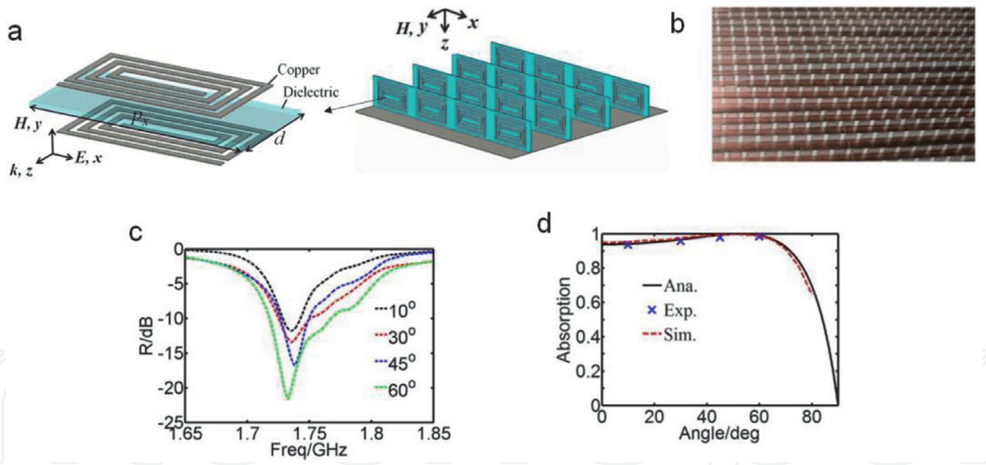

Figure 6.
(a) Sketch and (b) photo of an ultrathin perfect absorber based on magnetic resonant structures and its measured (c) reflection and (d) absorption.

function of the electric dipole array discussed above. The experimental results reported an absorption efficiency above 93% at 1.74 GHz at illumination angles up to 60 degrees [83]. Moreover, this absorber is 98% lighter than traditional microwave absorbers made of natural materials working at the same frequencies. As an alternative explanation, this structure can be seen as a metal-backed magnetic-near-zero (MNZ) metamaterial slab [84]. For an ultrathin metal-backed MNZ absorber, the permeability $\mu = (\mu' - j\mu'')\mu_0$ required for perfect absorption can be derived as: $\mu'\mu_0 \approx 0$ and $\mu''\mu_0 \approx 1/k_0 t$, where k_0 and μ_0 are the wavenumber and the permeability of free space, and t is the thickness of the metamaterial slab. This magnetic metamaterial absorber can achieve zero backward scattering (R = 0) and a large forward scattering (T = 0), i.e., $P_f = P_{inc}$ and $P_{ext} = P_a + P_s = 2P_{inc}$.

On the contrary, if symmetric designs are considered (e.g., a suspended resistive film with optimal sheet impedance $Z_s = \eta_0/2$ or a suspending epsilon-near-zero (ENZ) thin-slab with permittivity $\varepsilon = -j2/k_0 t$), only 50% of incident radiation can be absorbed. Due to the symmetric geometry and the negligible thickness of a resistive sheet/film, the induced surface current would equally re-radiate fields to

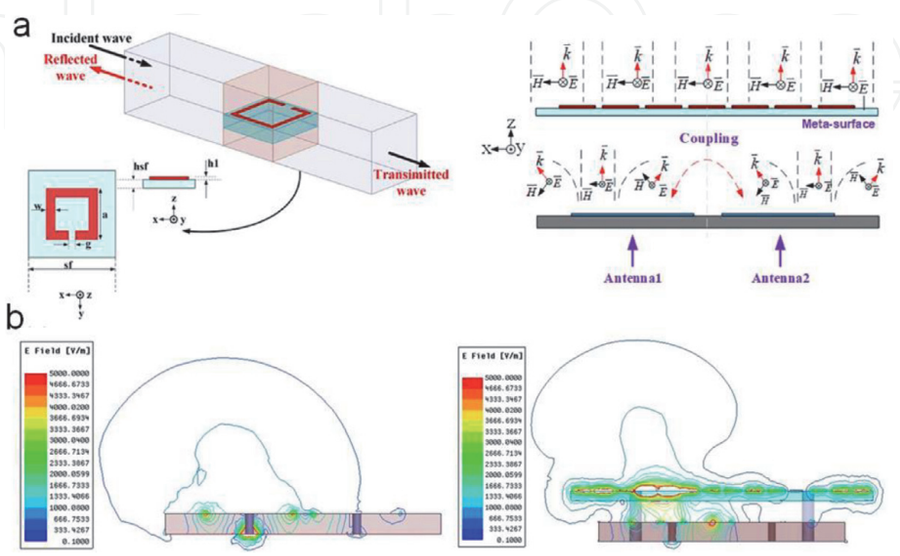

Figure 7.
(a) Magnetic metasurface for absorbing lateral radiation from the microstrip patch antenna. (b) Mutual coupling in a two-element MIMO system (left) without and (right) with the magnetic metasurface.

either side of the absorptive sheet, i.e., $P_r = P_f = |R|^2 P_{inc}$ leads to a maximum absorbed power $P_a = P_s = 0.5P_{inc}$ and thus $P_{ext} = P_{inc}$. Flat magnetic resonant structures have also been used to improve the isolation of MIMO antennas that are densely packed in a limited area. **Figure 7** shows a two-element array of rectangular patch antennas covered by the magnetic metasurface constituted by split-ring resonators [85]. From **Figure 7**, it is clearly seen that at the magnetic resonance, the resonators can effectively absorb the lateral radiation causing mutual coupling between antennas, thus effectively reducing the envelope correlation coefficient (ECC) of the MIMO system.

3. Hyperbolic metamaterial absorbers

Hyperbolic metamaterials (HMMs) (see **Figure 8**) are known for their isofrequency contour and broadband singularity in the density of photonic states, which have led to many new photonic and optical applications, including the substrate for molding spontaneous emissions into a directional beam and the "rainbow trapping" structure for broadband light absorption [25, 86–88]. The effective medium theory can describe the effective permittivity of such an artificial anisotropic medium as:

$$\bar{\bar{\varepsilon}}_{\text{eff}} = \varepsilon_0\left(\varepsilon_{\parallel}\hat{x}\hat{x} + \varepsilon_{\parallel}\hat{y}\hat{y} + \varepsilon_{\perp}\hat{z}\hat{z}\right), \tag{33}$$

$$\varepsilon_{\perp} = \left(\sum_{i=1}^{N} \varepsilon_i^{-1}\rho_i\right)^{-1}, \tag{34}$$

$$\varepsilon_{\parallel} = \sum_{i=1}^{N} \varepsilon_i \rho_i, \tag{35}$$

where ε_i and ρ_i are relative permittivity and volume fraction of i-*th* constituent materials, and ε_0 is the permittivity of free space. The isofrequency relation for the transverse-magnetic (TM) wave propagating in a uniaxially anisotropic medium, as schematically shown in **Figure 8**, can be expressed as

$$\frac{k_y^2 + k_z^2}{\varepsilon_{\perp}} + \frac{k_x^2}{\varepsilon_{\parallel}} = \frac{\omega^2}{c^2}. \tag{36}$$

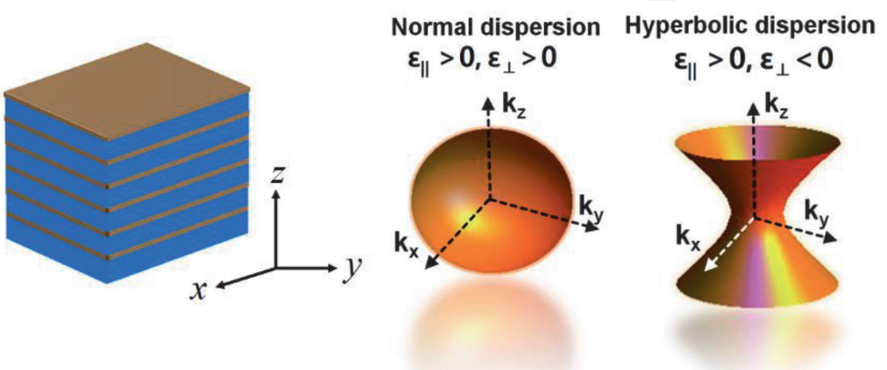

Figure 8.
Left: Schematics of HMM (left); right: Isofrequency surfaces of extraordinary waves in normal dielectrics and HMMs (right).

Therefore, for an anisotropic medium with extreme material properties, i.e., $\mathrm{Re}\left[\varepsilon_{\perp}\right] \cdot \mathrm{Re}\left[\varepsilon_{\parallel}\right] < 0$, the spherical isofrequency surface of vacuum distorts to an ellipsoid, as shown in **Figure 8**.

Figure 9a considers a trenched HMM slab with a periodicity P and air slots with width W, illuminated by a TM-polarized plane wave. The trenched HMM substrate is, in some sense, similar to a periodic array of air/HMM/air waveguides, for which a guided mode propagating along the waveguide axis can exhibit a near-zero group velocity, i.e., $v_g = \partial\omega/\partial\beta \approx 0$, at certain frequencies, where ω is the angular frequency and β is the modal propagation constant. With the periodic boundary conditions, the dispersion relation can be derived using the transverse resonance method [88–91] as:

$$\tan\left[\sqrt{k_0^2\varepsilon_{\perp} - \left(\varepsilon_{\perp}/\varepsilon_{\parallel}\right)\beta^2}\,\frac{P-W}{2}\right] - \varepsilon_{\perp}\frac{\sqrt{\beta^2 - k_0^2},}{\sqrt{k_0^2\varepsilon_{\perp} - \left(\varepsilon_{\perp}/\varepsilon_{\parallel}\right)\beta^2}}\tanh\left[\sqrt{\beta^2 - k_0^2},\,\frac{W}{2}\right] = 0 \tag{37}$$

where β is the modal propagation constant and k_0 is the free space wavenumber. Provided the periodicity of each MIM unit-cell is subwavelength ($P << \lambda_0$), all diffraction orders, except for the zero*th* mode, are evanescent. The scattering and absorption properties of this HMM-based device can be solved using the TL model (TLM) and the transfer matrix method (TMM), as shown in **Figure 9**. For the TM-wave illumination normally incident upon the HMM substrate, the characteristic impedance per unit length can be expressed as $Z_0 = V_0/I_0 = \int_0^{P/2} E_x dx/H_y = \eta_0 P/2$, which is defined as the ratio between the voltage across one period $V_0 = \int_0^{P/2} E_x dx = |\mathbf{E}_0| d\cos\theta$ and the current per unit length $I_0 = H_y = \varepsilon_0 c|\mathbf{E}_0|$, where ε_0 and c are permittivity and speed of light in free space. Similarly, the characteristic

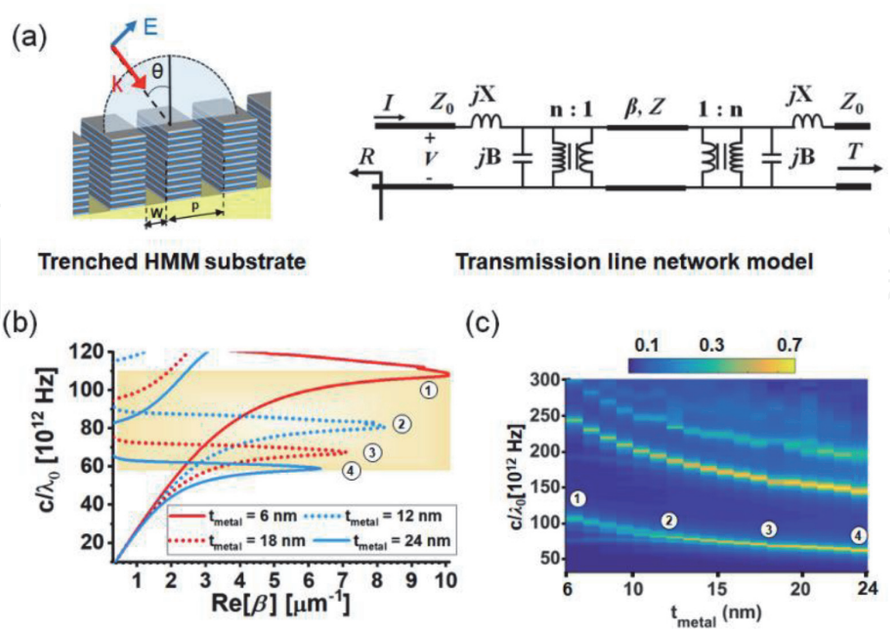

Figure 9.
(a) Schematics of a slow-light structure based on the structured HMM that can be described using a transmission line network model. (b) Dispersion diagram for a waveguide array made by carving an HMM substrate made of repeated Ag-NbO-Cu lattices with P = 300 *nm and* W = 100 *nm. Labels in (a) and (b) indicate the slow-wave modes and the corresponding absorption peaks. (c) Calculated contours of absorptance for the HMM in (b) constituted by* 12 *MIM heterojunctions, varying the metal thickness* (t_{metal}) *and the operating wavelength; [89].*

impedance of HMM $Z = (\beta/\omega\varepsilon_0) \times (W/2)$. At the interface between air and metasurface, there exists a shunt surface susceptance B imposed by the discontinuous fields [92].

$$B = \frac{2P}{\lambda_0}\left(\log\left[\frac{1-\alpha^2}{4\alpha}\left(\frac{1+\alpha}{1-\alpha}\right)^{\frac{\alpha+\alpha^{-1}}{2}}\right] + 2\frac{C_1+C_2+2C_3}{C_1C_2-C_3^2} + \left(\frac{P}{4\lambda_0}\right)^2\left(\frac{1-\alpha}{1+\alpha}\right)^{4\alpha}\left(\frac{5\alpha^2-1}{1-\alpha^2}+\frac{4}{3}\frac{\alpha^2C_3}{C_1}\right)^2\right), \tag{38}$$

$$\begin{aligned} C_1 &= \left(\frac{1+\alpha}{1-\alpha}\right)^{2\alpha}\frac{1+\sqrt{1-(P/\lambda_0)^2}}{1-\sqrt{1-(P/\lambda_0)^2}} - \frac{1+3\alpha^2}{1-\alpha^2}, \\ C_2 &= \left(\frac{1+\alpha}{1-\alpha}\right)^{2/\alpha}\frac{1+\sqrt{1-(W/\lambda_0)^2}}{1-\sqrt{1-(W/\lambda_0)^2}} + \frac{3+\alpha^2}{1-\alpha^2}, \\ C_3 &= \left(\frac{4\alpha}{1-\alpha^2}\right)^2, \end{aligned} \tag{39}$$

and $\alpha = W/P$. The reflection/transmission spectrum and absorption peaks can be calculated based on the TLM mode shown in **Figure 9**.

Figure 9b shows the calculated dispersion diagram of a periodically trenched HMM slab constituted by stacked silver (Ag) and copper (Cu) thin-films with thickness t_{metal}, separated by 1 nm-thick niobium oxide (Nb_2O_5) insulating layers, of which the periodicity and air gap size are 300 nm and 150 nm, respectively. The realistic material properties extracted from experiments are used [89]. It can be seen from **Figure 9b** that near-zero group velocity can be achieved at certain wavelengths, resulting in the slow light effect and light trapping and absorption in the lossy (dissipative plasmon loss) and anisotropic HMM region. **Figure 9c** presents the associated contour plot of absorptance as a function of metal thickness t_{metal} [nm] and wavelength λ [μm]. We find excellent agreement between the wavelengths of maximum absorption in **Figure 9c** and the near-zero group velocity points in the dispersion diagram plotted in **Figure 9b**. We note that total HMM size is still subwavelength since the large value of $\mathrm{Re}[\beta]$ suggests that the incident light can be effectively absorbed in a long-wavelength range.

Additionally, the absorption spectrum can be readily tailored by varying the volume fraction of metal, which determines the permittivity tensor elements of HMM. Although a linear HMM-based absorber can exhibit a high and angle-independent optical absorption, its bandwidth is limited around the slow-wave modes. This limitation can be mitigated by exploiting a tapered-HMM, as shown in **Figure 10a**, which has been proposed to realize wideband photodetection and solar energy harvesting applications [88–91]. Using tapered geometry, the bandwidth is expected to increase due to the superposition of multiple slow-wave modes. Figure **Figure 10b** shows the contour plot of absorptance as a function of the photon energy and the angle of incidence. It is evidently seen that a broadband (1 eV to 1.6 eV) and wide-angle (0° to grazing angle) optical absorption can be obtained with the tapered HMM substrate backed by a metallic mirror (50 nm Ag thin-film). The capability to effectively trap photons over a wide range of photon energies and illumination angles is essential for building efficient hot-electron energy harvesters or photodetectors. Finally, we note that the general limitation on the maximum bandwidth of a ground-backed absorber should always obey the passivity and causality [93], following the physical bound $\left|\int_0^\infty \ln|r(\hbar\omega)|\mathrm{d}\hbar\omega\right| \le 2\pi^2\sum_i \mu_{s,i}t_i/\mu_0$,

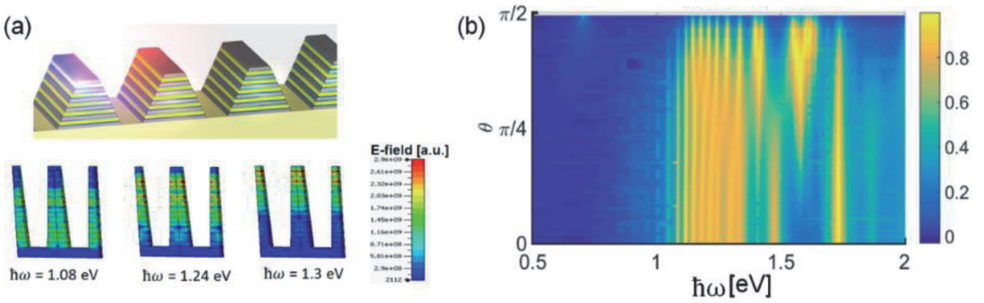

Figure 10.
(a) Top: Schematics of the HMM with a periodic array of tapered trenches, which allows one to tailor the broadband of light trapping; bottom: Snapshots of electric field distributions inside the tapered HMM at photon energies of 260 THz, 300 THz, and 320 THz (left to right). (b) Contour of absorptance as a function of photon energy and incident angle for the tapered-HMM [88].

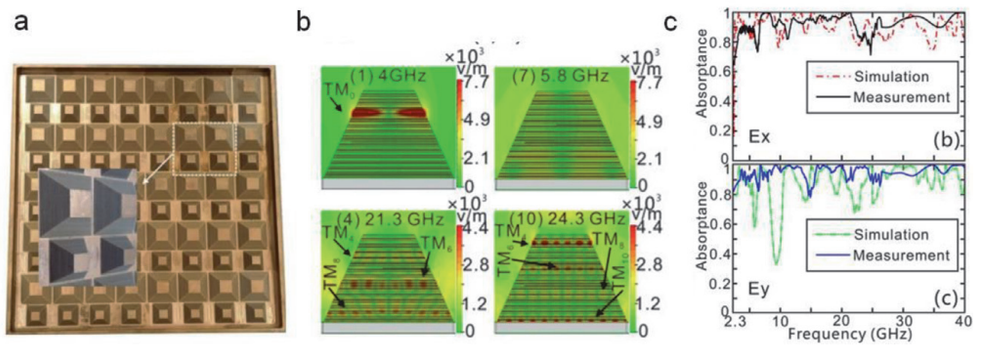

Figure 11.
(a) Photograph of a microwave HMM absorber. (b) Simulated electric field distributions at different frequencies. (c) Measured absorption spectra for different polarizations.

where $r(\hbar\omega)$ is the reflection coefficient as a function of photon energy, $\mu_{s,i}$ and t_i are the static permeability and the thickness of the i-*th* layer of the multilayered absorptive slab. For an effective non-magnetic medium, we can define Rozanov's limiting factor as $\eta_{Rozanov} = \left|\int_0^\infty \ln|r(\hbar\omega)|d\,\hbar\omega\right|/2\pi^2 t$, where t is the total thickness of the absorber. $\eta_{Rozanov}$ must be less than unity and a larger value corresponds to a wider absorption bandwidth. For the tapered HMM in **Figure 10b**, the calculated $\eta_{Rozanov}$ can reach ~40%, which, although not optimized yet, is moderately high for the polarized light.

Similarly, an ultra-broadband HMM absorber can be realized in the RF and microwave regions by integrating two different-sized tapered HMM waveguides, as shown in **Figure 11a** [94], each of which has wide but different absorption bands, leading to a broadband slow-light response. By properly selecting the geometrical parameters for each waveguide in the HMM, multiple absorption bands can be achieved with different waveguides, as shown in **Figure 11b**. Such an approach can effectively widen the total absorption bandwidth. Experimental results in Ref. [94] validate the theoretical results, showing a very large absorption bandwidth ranging from 2.3 GHz to 40 GHz.

4. Future trends: reconfigurable absorbers based on plasmonic, graphene, and beyond

Electromagnetic wave absorbers are mainly utilized as boundary structures to prevent the scattering of electromagnetic fields. They can be divided into two main

categories based on their operating bandwidth, i.e., resonant and broadband absorbers [95, 96]. Resonant absorbers typically depend on the designed material assemblies interrelating with the incident waves around certain resonance frequencies [96]. On the other hand, the wideband absorbers rely on material damping characteristics that are largely independent of electromagnetic frequencies and typically made of lossy dispersive materials [96]. Such broadband absorbing materials along with structural transition are commonly used in anechoic chambers to effectively emulate a non-reflecting unbounded medium suitable for testing radiating antenna elements [95]. Lately, there is an emphasis in the scientific community to design efficient plasmonic metamaterial-based absorbers. Light matter interaction in subwavelength metamaterial structures allowed various other applications including perfect lenses [45, 97], chiral surfaces [98, 99], transformational surfaces [100, 101], optical cloaking [100, 102, 103], spatial light switching [104, 105] and IR camouflage and microwave antennas because of certain useful characteristics [96]. In addition to these applications, the perfect metamaterial absorber (PMA) is designed as a tool to efficiently absorb electromagnetic waves utilizing plasmonic resonator elements embedded within its assembly.

Generally, metamaterial absorbers are composed of a patterned metal film over a continuous thin metallic film with a dielectric substrate sandwiched between them [96]. It should be noted that the definition of total absorptivity considers reflected electric field vector, i.e., $\vec{\mathbf{R}} = R_{ii}\hat{\boldsymbol{a}}_i + R_{ji}\hat{\boldsymbol{a}}_j$, that considers both co- ($R_{ii} = E_i^{ref}/E_i^{inc}$) and cross ($R_{ji} = E_j^{ref}/E_i^{inc}$) polarized components of reflected fields [21]. Here, subscript $\{i,j\} = \{x,y\}$refer to x or y coordinates. Oftentimes, the plasmonic metasurface absorbers inhibits only co- polarized reflection (i.e., $R_{ii} = 0$) and converts incident fields to cross polarized reflected fields components (R_{ji}) [21, 106], as shown in **Figure 12**. Such metasurface is designed with certain structural anisotropy that allows the flow of electric currents that suppresses co- polarization states (R_{ii}) for the reflected fields. As a result, such plasmonic metasurface converts the polarization of incident electromagnetic fields to orthogonal reflected field component (R_{ji}). Special cases of circular or elliptical polarized reflected fields may also be attained by specific vector combination of co- (R_{ii}) and cross (R_{ji}) polarized components [107, 108]. In the case of a full absorber as shown in **Figure 12(a)**, the normalized perfect absorption $A(\omega)$ due to the plasmonic metasurface can be found from the amplitude of reflected fields i.e., $A(\omega) = 1 - |R(\omega)|^2 - |T(\omega)|^2$. Here,

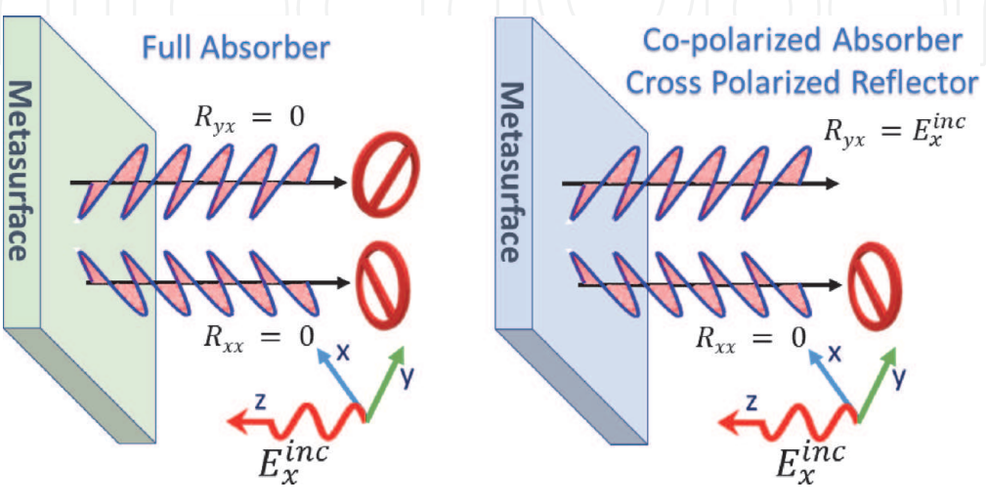

Figure 12.
(Left) full absorber to inhibit any scattering from the metasurface. (Right) cross polarizer to suppress the co-polarized component ($R_{xx} = 0$) while not affecting cross-polarized reflection component (R_{yx}).

$|R(\omega)|$ and $|T(\omega)|$ are amplitudes of reflected and transmitted fields, respectively. The ideal back reflector typically supports negligible transmission i.e., $|T(\omega)| = 0$.

The response of PMA is often described as an effective medium and characterized by properties such as complex electric permittivity (ε) and magnetic permeability (μ) [109]. Although much of the work on effective medium properties of metamaterials has been focused on the real part of ε and μ, as it contributes to negative refractive index properties, it is equally important to reduce losses represented by the imaginary part of ε and μ for practical applications related to wave propagation within negative refractive index medium [110, 111]. In contrast, the metamaterial absorbers rely on high material losses (large value of imaginary parts of ε and μ) and impedance matching with the background medium. Landy et al. provided the first experimental demonstration of near perfect metasurface absorption at GHz frequencies. The working principle of PMA relies on impedance matching between effective medium forming metasurface with dielectric and background medium to the free space background, rejecting the reflection and therefore efficiently absorbing the incident EM wave [19, 20]. Ever since, the design of PMAs has attracted significant attention ranging from microwave to optical frequencies [112, 113]. Apart from resonant absorption characteristics, the plasmonic effects also provide tremendous near field enhancement to improve the efficiency of solar cells [114], support for sensing [31], and enhanced thermal emission and photo-detection [115].

Recently, the electro-optic tunability of resonant absorption spectrum at THz frequencies is made possible by varying the frequency dependent conductivity of plasmonic materials through the use of graphene metasurface [22, 59]. The frequency dependent optical properties of graphene in the THz frequency range are controlled by its optoelectronic properties. The permittivity (ε_g) of graphene is function of the surface conductivity (σ_g).

$$\varepsilon_g(\omega) = 1 + j\frac{\sigma_g(\omega)}{\varepsilon_0 \omega \Delta}. \tag{40}$$

Here, ε_0 is the vacuum permittivity, and Δ = 1 nm is the monoatomic thickness of graphene.

The surface conductivity of graphene (σ_g) can be deduced from the Kubo formula, at low THz frequencies (inter-band conductivity can be neglected in this regime),

$$\sigma_g(\omega) = j\frac{e_0^2 k_B T}{\pi\hbar(\hbar\omega + j\Gamma)}\left\{\frac{\mu_c}{k_B T} + 2\log\left[1 + e^{-\mu_c/(k_B T)}\right]\right\}. \tag{41}$$

Here, μ_c[eV] is the chemical potential of graphene, $\Gamma = -\left(e_0\hbar v_f^2\right)/(\mu\mu_c)$ is the damping coefficient, v_f [m/s] is the Fermi velocity, and μ [cm^2/Vs] is the electron mobility, e_0 is the electronic unit-charge, T is temperature, k_B is the Boltzmann constant, and $\hbar$ is the reduced Plank's constant. Therefore, the surface conductivity σ_g and permittivity of graphene ε_g can be directly controlled by varying μ_c. The chemical potential can be controlled by doping graphene or by applying an electrostatic bias to the graphene sheet.

The real-time tunability of Graphene Surface Plasmons (GSPs) is a distinct feature offered by graphene metasurface when compared to traditional noble metals. In addition, GSPs offer other benefits such as tighter mode volume confinement and lower intrinsic losses compared to conventional surface plasmon materials. The unique electro-optic tunability of graphene conductivity within the THz

band makes it an attractive candidate for plasmonic metamaterial applications. Therefore, graphene enabled the research in surface plasmons to be redirected toward reconfigurable THz wave optics applications, including GSPP waveguides [116], modulators [24], THz cloaks [117], THz antennas [118], Fourier optics [119], photonic crystal nano-cavities [120], and biochemical sensors [31, 121]. The reconfigurable response of resonant absorption can offer additional functionalities, including wave modulation, polarization conversion, and sensing.

Here, we discuss a few selected applications of reconfigurable THz metasurface absorbers, as shown in **Figure 13**. **Figure 13(a)** shows graphene micro-ribbon metasurface design capable of efficiently absorbing THz radiation [22]. The chemical potential (μ_c) can be used to control graphene conductivity. As a result, the

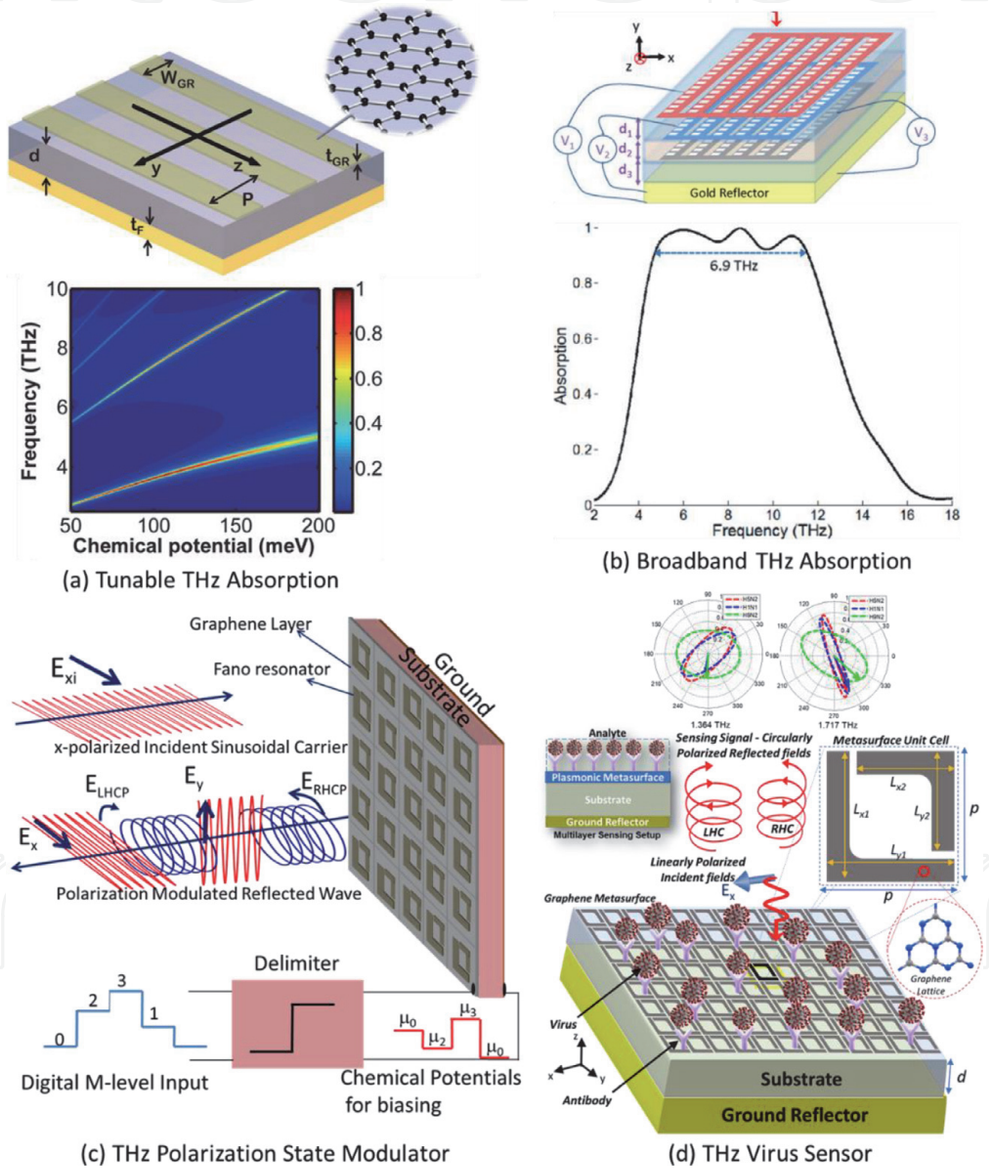

Figure 13.
(a) (Top) Schematic illustration of graphene micro-ribbon metasurface. (Bottom) Tunable absorption characteristics due to variation in graphene chemical potential (μ_c) [22]. (b) (Top) Multilayer graphene metasurface biased at different levels to efficiently absorb incident radiation. (Bottom) Wideband absorption spectrum for THz waves for the normal incident condition [59]. (c) Description of polarization state modulation of a digital M-level signal by chiral graphene metasurface. The 4-level digital stream is fed to a limiter that converts it into the required chemical potential and consequently produces desired polarization state for the reflected field [98]. (d) The chiral biosensor is constructed by graphene metasurface supporting chiral reflection characteristics to test ligand-antigen bindings on the surface. The resonance frequency supports a distinct contour path traversed by locus tip of electric field vector in time for three different strains of influenza viruses H1N1, H5N2, and H9N2 [31].

reconfigurable response with near perfect absorption can be utilized for THz wave modulation applications. **Figure 13(b)** shows a design of multilayer graphene metasurface that operates at THz frequencies [59]. The graphene layers are designed to generate quadrupolar localized surface plasmons that destructively interfere with the dipole mode. The patterned graphene layers are biased to operate at different chemical potential levels and backed up with dielectric substrates stacked on top of each other. Full-wave electromagnetic simulations demonstrate that the absorption spectrum is not only tunable but can be optimized to a large bandwidth of operation, *i.e.*, 6.9 THz bandwidth is obtained for over 90% normalized absorption. **Figure 13(c)** shows a schematic illustration of the design of graphene metasurface supporting polarization state modulation with high spectral efficiency [98]. The structural chirality of metasurface is utilized to generate chiral reflection along with highly dispersive Fano resonance. Several polarization states, including two orthogonal linearly polarized, right-and left-handed circular polarized reflections, are demonstrated for a narrow electro-optic tuning range of chemical potentials between 500 and 700 meV. By exploiting these properties, highly efficient modulation stages of modern communication systems can be designed. **Figure 13(d)** shows a polarization-state sensing setup to distinguish closely resembling optical properties of biomolecules such as viruses [31]. The measurement consists of a plasmonic metasurface with chiral unit cells, and the polarization properties of reflected fields can determine the optical characteristics of the analyte. It is shown that the proposed sensor can distinguish three closely resembling influenza virus strains i.e., H1N1, H5N2, and H9N2 based on the variation of the reflected polarization states.

5. Conclusion

In this chapter, we have reviewed the most recent advances in the field of metamaterial and metasurface-based electromagnetic perfect absorbers. We have first provided a thorough theoretical investigation describing the material and geometrical conditions that may lead to a near-perfect absorption of light. Based on the well-known optical theorem, this analysis gives a power balance and clarifies the design process in the microwaves and terahertz. Next, we have discussed a peculiar and interesting class of perfect absorbers that are hyperbolic metamaterial absorbers. These devices exploit a particular dispersion of hyperbolic media and lead to robust and tunable absorbers. We finally have discussed the newly proposed graphene plasmonics based absorbers, which exploit the high conductivity and tunable optical properties of this 2D material to build some of the most appealing and versatile absorbers, with applications spanning energy harvesting, biosensing, or light polarization manipulation. This chapter can be helpful to theorists and experimentalists alike, working on the design of novel absorbers of light or even other types of waves.

Author details

Pai-Yen Chen[1*], Mohamed Farhat[2], Zhilu Ye[1], Muhammad Amin[3], Hakan Bagci[1] and Danilo Erricolo[2]

1 Department of Electrical and Computer Engineering, University of Illinois Chicago, Chicago, IL, USA

2 Computer, Electrical, and Mathematical Science and Engineering (CEMSE) Division, King Abdullah University of Science and Technology (KAUST), Thuwal, Saudi Arabia

3 College of Engineering, Taibah University, Madinah, Saudi Arabia

*Address all correspondence to: pychen@uic.edu

References

[1] Mishra N, Kumari K, Chaudhary RK. An ultra-thin polarization independent quad-band microwave absorber-based on compact metamaterial structures for EMI/EMC applications. Int. J. Microw. Wireless Technol. 2018;**10**:422

[2] Holloway CL, DeLyser RR, German RF, McKenna P, Kanda M. Comparison of electromagnetic absorber used in anechoic and semi-anechoic chambers for emissions and immunity testing of digital devices. IEEE Transactions on Electromagnetic Compatibility. 1997;**39**:33

[3] Crawford ML, Workman JL, Thomas CL. Expanding the Bandwidth of TEM Cells for EMC Measurements. IEEE Transactions on Electromagnetic Compatibility. 1978;**EMC-20**:368

[4] Groh C, Karst JP, Koch M, Garbe H. TEM waveguides for EMC measurements. IEEE Transactions on Electromagnetic Compatibility. 1999;**41**: 440

[5] Mishra SR, Pavlasek TJF. Design of Absorber-Lined Chambers for EMC Measurements Using a Geometrical Optics Approach. IEEE Transactions on Electromagnetic Compatibility. 1984; **EMC-26**:111

[6] L. Zhao, H. Liu, Z. He, and S. Dong, All-metal frequency-selective absorber/ emitter for laser stealth and infrared stealth, Appl. Opt., AO **57**, 1757 (2018).

[7] Panwar R, Puthucheri S, Singh D, Agarwala V. Design of Ferrite–Graphene-Based Thin Broadband Radar Wave Absorber for Stealth Application. IEEE Transactions on Magnetics. 2015;**51**:1

[8] Chakradhary VK, Baskey HB, Roshan R, Pathik A, Akhtar MJ. Design of Frequency Selective Surface-Based Hybrid Nanocomposite Absorber for Stealth Applications. IEEE Transactions on Microwave Theory and Techniques. 2018;**66**:4737

[9] Kim J, Han K, Hahn JW. Selective dual-band metamaterial perfect absorber for infrared stealth technology. Scientific Reports. 2017;**7**:6740

[10] Kim T, Bae J, Lee N, Cho HH. Hierarchical Metamaterials for Multispectral Camouflage of Infrared and Microwaves. Adv. Funct. Mater. 2019;**29**:1807319

[11] Sabah C, Dincer F, Karaaslan M, Unal E, Akgol O, Demirel E. Perfect metamaterial absorber with polarization and incident angle independencies based on ring and cross-wire resonators for shielding and a sensor application. Optics Communications. 2014;**322**:137

[12] Gholampoor M, Movassagh-Alanagh F, Salimkhani H. Fabrication of nano-Fe3O4 3D structure on carbon fibers as a microwave absorber and EMI shielding composite by modified EPD method. Solid State Sciences. 2017;**64**:51

[13] Micheli D, Apollo C, Pastore R, Bueno Morles R, Laurenzi S, Marchetti M. Nanostructured composite materials for electromagnetic interference shielding applications. Acta Astronautica. 2011;**69**:747

[14] Farhat M, Chen P-Y, Bagci H, Amra C, Guenneau S, Alù A. Thermal invisibility based on scattering cancellation and mantle cloaking. Scientific Reports. 2015;**5**:9876

[15] Dincer F. Electromagnetic energy harvesting application based on tunable perfect metamaterial absorber. Journal of Electromagnetic Waves and Applications. 2015;**29**:2444

[16] Chung BK, Chuah HT. Design and construction of a multipurpose

wideband anechoic chamber. IEEE Antennas and Propagation Magazine. 2003;**45**:41

[17] S. F. Gregson, J. Dupuy, C. G. Parini, A. C. Newell, and G. E. Hindman, in 2011 Loughborough Antennas Propagation Conference (2011), pp. 1–4.

[18] Qu Y, Li Q, Gong H, Du K, Bai S, Zhao D, et al. Spatially and Spectrally Resolved Narrowband Optical Absorber Based on 2D Grating Nanostructures on Metallic Films. Advanced Optical Materials. 2016;**4**:480

[19] Landy NI, Sajuyigbe S, Mock JJ, Smith DR, Padilla WJ. Perfect Metamaterial Absorber. Phys. Rev. Lett. 2008;**100**:207402

[20] Tao H, Landy NI, Bingham CM, Zhang X, Averitt RD, Padilla WJ. A metamaterial absorber for the terahertz regime: Design, fabrication and characterization, Opt. Express, OE. 2008;**16**(7181)

[21] B.-Y. Wang, S.-B. Liu, B.-R. Bian, Z.-W. Mao, X.-C. Liu, B. Ma, and L. Chen, A novel ultrathin and broadband microwave metamaterial absorber, Journal of Applied Physics **116**, 094504 (2014).

[22] Alaee R, Farhat M, Rockstuhl C, Lederer F. A perfect absorber made of a graphene micro-ribbon metamaterial, Opt. Express, OE. 2012;**20**(28017)

[23] Cao T, Wei C, Simpson RE, Zhang L, Cryan MJ. Broadband Polarization-Independent Perfect Absorber Using a Phase-Change Metamaterial at Visible Frequencies. Scientific Reports. 2014;**4**:3955

[24] Zhang Y, Feng Y, Zhu B, Zhao J, Jiang T. Graphene based tunable metamaterial absorber and polarization modulation in terahertz frequency, Opt. Express, OE. 2014;**22**(22743)

[25] Zhou J, Kaplan AF, Chen L, Guo LJ. Experiment and Theory of the Broadband Absorption by a Tapered Hyperbolic Metamaterial Array. ACS Photonics. 2014;**1**:618

[26] D. Chaurasiya, S. Ghosh, S. Bhattacharyya, and K. V. Srivastava, in 2014 IEEE International Microwave and RF Conference (IMaRC) (2014), pp. 96–99.

[27] Singh AK, Abegaonkar MP, Koul SK. A Triple Band Polarization Insensitive Ultrathin Metamaterial Absorber for S- C- and X-Bands. Progress In Electromagnetics Research M. 2019;**77**: 187

[28] W. Li, X. Zhou, Y. Ying, X. Qiao, F. Qin, Q. Li, and S. Che, Polarization-insensitive wide-angle multiband metamaterial absorber with a double-layer modified electric ring resonator array, AIP Advances **5**, 067151 (2015).

[29] Liu T, Cao X, Gao J, Zheng Q, Li W, Yang H. RCS Reduction of Waveguide Slot Antenna With Metamaterial Absorber. IEEE Transactions on Antennas and Propagation. 2013;**61**: 1479

[30] Luo S, Zhao J, Zuo D, Wang X. Perfect narrow band absorber for sensing applications, Opt. Express, OE. 2016;**24**(9288)

[31] Amin M, Siddiqui O, Abutarboush H, Farhat M, Ramzan R. A THz graphene metasurface for polarization selective virus sensing. Carbon. 2021;**176**:580

[32] Liu N, Mesch M, Weiss T, Hentschel M, Giessen H. Infrared Perfect Absorber and Its Application As Plasmonic Sensor. Nano Lett. 2010;**10**: 2342

[33] Zhang L, Farhat M, Salama KN. Spectrometer-Free Graphene

Plasmonics Based Refractive Index Sensor. Sensors. 2020;**20**:2347

[34] Landy NI, Bingham CM, Tyler T, Jokerst N, Smith DR, Padilla WJ. Design, theory, and measurement of a polarization-insensitive absorber for terahertz imaging. Phys. Rev. B. 2009; **79**:125104

[35] Chen P-Y, Alù A. Subwavelength Imaging Using Phase-Conjugating Nonlinear Nanoantenna Arrays. Nano Lett. 2011;**11**:5514

[36] Wesemann L, Panchenko E, Singh K, Della Gaspera E, Gómez DE, Davis TJ, et al. Selective near-perfect absorbing mirror as a spatial frequency filter for optical image processing. APL Photonics. 2019;**4**:100801

[37] Sharawi MS, Numan AB, Khan MU, Aloi DN. A Dual-Element Dual-Band MIMO Antenna System With Enhanced Isolation for Mobile Terminals. IEEE Antennas and Wireless Propagation Letters. 2012;**11**:1006

[38] Zhang S, Ying Z, Xiong J, He S. Ultrawideband MIMO/Diversity Antennas With a Tree-Like Structure to Enhance Wideband Isolation. IEEE Antennas and Wireless Propagation Letters. 2009;**8**:1279

[39] Jackson JD. Classical Electrodynamics. 3rd ed. New York: Wiley; 1999

[40] Pendry JB, Holden AJ, Robbins DJ, Stewart WJ. Magnetism from conductors and enhanced nonlinear phenomena. IEEE Transactions on Microwave Theory and Techniques. 1999;**47**:2075

[41] D. M. Pozar, Microwave Engineering (John Wiley & Sons, 2011).

[42] H. W. Ott, Electromagnetic Compatibility Engineering (John Wiley & Sons, 2011).

[43] J. D. Baena, R. Marqués, F. Medina, and J. Martel, Artificial magnetic metamaterial design by using spiral resonators, Phys. Rev. B **69**, 014402 (2004).

[44] Bilotti F, Toscano A, Vegni L, Aydin K, Alici KB, Ozbay E. Equivalent-Circuit Models for the Design of Metamaterials Based on Artificial Magnetic Inclusions. IEEE Transactions on Microwave Theory and Techniques. 2007;**55**:2865

[45] Pendry JB. Negative Refraction Makes a Perfect Lens. Phys. Rev. Lett. 2000;**85**:3966

[46] Shelby RA, Smith DR, Schultz S. Experimental Verification of a Negative Index of Refraction. Science. 2001;**292**: 77

[47] Schurig D, Mock JJ, Justice BJ, Cummer SA, Pendry JB, Starr AF, et al. Metamaterial Electromagnetic Cloak at Microwave Frequencies. Science. 2006; **314**:977

[48] M. Farhat, P.-Y. Chen, S. Guenneau, and S. Enoch, Transformation Wave Physics: Electromagnetics, Elastodynamics, and Thermodynamics (CRC Press, 2016).

[49] S. A. Maier, Plasmonics: Fundamentals and Applications (Springer Science & Business Media, 2007).

[50] Brolo AG. Plasmonics for future biosensors. Nature Photonics. 2012;**6**:709

[51] Xiao S, Liu L, Qiu M. Resonator channel drop filters in a plasmon-polaritons metal, Opt. Express, OE. 2006;**14**(2932)

[52] Liu Y, Cheng R, Liao L, Zhou H, Bai J, Liu G, et al. Plasmon resonance enhanced multicolour photodetection by graphene. Nature Communications. 2011;**2**:579

[53] Ma R-M, Oulton RF, Sorger VJ, Bartal G, Zhang X. Room-temperature sub-diffraction-limited plasmon laser by total internal reflection. Nature Materials. 2011;**10**:110

[54] C. Argyropoulos, P.-Y. Chen, G. D'Aguanno, N. Engheta, and A. Alù, Boosting optical nonlinearities in $ \ensuremath{\epsilon}$-near-zero plasmonic channels, Phys. Rev. B **85**, 045129 (2012).

[55] Grosjean T, Mivelle M, Baida FI, Burr GW, Fischer UC. Diabolo Nanoantenna for Enhancing and Confining the Magnetic Optical Field. Nano Lett. 2011;**11**:1009

[56] Kildal P-S, Alfonso E, Valero-Nogueira A, Rajo-Iglesias E. Local Metamaterial-Based Waveguides in Gaps Between Parallel Metal Plates. IEEE Antennas and Wireless Propagation Letters. 2009;**8**:84

[57] Teperik TV, García de Abajo FJ, Borisov AG, Abdelsalam M, Bartlett PN, Sugawara Y, et al. Omnidirectional absorption in nanostructured metal surfaces. Nature Photonics. 2008; **2**:299

[58] Y. D. Chong, L. Ge, H. Cao, and A. D. Stone, Coherent Perfect Absorbers: Time-Reversed Lasers, Phys. Rev. Lett. **105**, 053901 (2010).

[59] Amin M, Farhat M, Bağcı H. An ultra-broadband multilayered graphene absorber, Opt. Express, OE. 2013;**21** (29938)

[60] Aalizadeh M, Khavasi A, Butun B, Ozbay E. Large-Area, Cost-Effective, Ultra-Broadband Perfect Absorber Utilizing Manganese in Metal-Insulator-Metal Structure. Scientific Reports. 2018;**8**:9162

[61] Rephaeli E, Fan S. Absorber and emitter for solar thermo-photovoltaic systems to achieve efficiency exceeding the Shockley-Queisser limit, Opt. Express, OE. 2009;**17**(15145)

[62] M. Diem, T. Koschny, and C. M. Soukoulis, Wide-angle perfect absorber/thermal emitter in the terahertz regime, Phys. Rev. B **79**, 033101 (2009).

[63] M. Kerker, The Scattering of Light and Other Electromagnetic Radiation: Physical Chemistry: A Series of Monographs (Academic Press, 2013).

[64] Kwon D-H, Pozar DM. Optimal Characteristics of an Arbitrary Receive Antenna. IEEE Transactions on Antennas and Propagation. 2009;**57**:3720

[65] Fante RL, McCormack MT. Reflection properties of the Salisbury screen. IEEE Transactions on Antennas and Propagation. 1988;**36**:1443

[66] Chen P-Y, Argyropoulos C, D'Aguanno G, Alù A. Enhanced Second-Harmonic Generation by Metasurface Nanomixer and Nanocavity. ACS Photonics. 2015;**2**:1000

[67] A. Alù, First-principles homogenization theory for periodic metamaterials, Phys. Rev. B **84**, 075153 (2011).

[68] S. Tretyakov, Analytical Modeling in Applied Electromagnetics (Artech House, 2003).

[69] P. A. Belov and C. R. Simovski, Homogenization of electromagnetic crystals formed by uniaxial resonant scatterers, Phys. Rev. E **72**, 026615 (2005).

[70] G. N. Watson, A Treatise on the Theory of Bessel Functions (Cambridge University Press, 1995).

[71] M. Abramowitz and I. A. Stegun, Handbook of Mathematical Functions with Formulas, Graphs, and Mathematical Tables (U.S. Government Printing Office, 1964).

[72] Simovski CR, Zouhdi S, Yatsenko VV. Electromagnetic interaction in dipole grids and prospective high-impedance surfaces. Radio Science. 2005;**40**:1

[73] Smith DR, Padilla WJ, Vier DC, Nemat-Nasser SC, Schultz S. Composite Medium with Simultaneously Negative Permeability and Permittivity. Phys. Rev. Lett. 2000;**84**:4184

[74] D. R. Smith, J. Gollub, J. J. Mock, W. J. Padilla, and D. Schurig, Calculation and measurement of bianisotropy in a split ring resonator metamaterial, Journal of Applied Physics **100**, 024507 (2006).

[75] T. Driscoll, G. O. Andreev, D. N. Basov, S. Palit, S. Y. Cho, N. M. Jokerst, and D. R. Smith, Tuned permeability in terahertz split-ring resonators for devices and sensors, Appl. Phys. Lett. **91**, 062511 (2007).

[76] A. K. Azad, A. J. Taylor, E. Smirnova, and J. F. O'Hara, Characterization and analysis of terahertz metamaterials based on rectangular split-ring resonators, Appl. Phys. Lett. **92**, 011119 (2008).

[77] Rockstuhl C, Zentgraf T, Guo H, Liu N, Etrich C, Loa I, et al. Resonances of split-ring resonator metamaterials in the near infrared. Appl. Phys. B. 2006; **84**:219

[78] Le KQ, Bai J, Ngo QM, Chen P-Y. Fabrication and Numerical Characterization of Infrared Metamaterial Absorbers for Refractometric Biosensors. Journal of Elec Materi. 2017;**46**:668

[79] X. Zhao, J. Zhang, K. Fan, G. Duan, G. D. Metcalfe, M. Wraback, X. Zhang, and R. D. Averitt, Nonlinear terahertz metamaterial perfect absorbers using GaAs [Invited], Photon. Res., PRJ **4**, A16 (2016).

[80] Asadchy VS, Díaz-Rubio A, Tretyakov SA. Bianisotropic metasurfaces: physics and applications. Nanophotonics. 2018;**7**:1069

[81] Liang F, Hanson GW, Yakovlev AB, Lovat G, Burghignoli P, Araneo R, et al. Dyadic Green's Functions for Dipole Excitation of Homogenized Metasurfaces. IEEE Transactions on Antennas and Propagation. 2016;**64**:167

[82] Yatsenko VV, Maslovski SI, Tretyakov SA, Prosvirnin SL, Zouhdi S. Plane-wave reflection from double arrays of small magnetoelectric scatterers. IEEE Transactions on Antennas and Propagation. 2003;**51**:2

[83] Zhong S, He S. Ultrathin and lightweight microwave absorbers made of mu-near-zero metamaterials. Scientific Reports. 2013;**3**:2083

[84] Chen P-Y, Farhat M, Bağcı H. Graphene metascreen for designing compact infrared absorbers with enhanced bandwidth. Nanotechnology. 2015;**26**:164002

[85] Wang Z, Zhao L, Cai Y, Zheng S, Yin Y. A Meta-Surface Antenna Array Decoupling (MAAD) Method for Mutual Coupling Reduction in a MIMO Antenna System. Scientific Reports. 2018;**8**:3152

[86] Poddubny A, Iorsh I, Belov P, Kivshar Y. Hyperbolic metamaterials. Nature Photonics. 2013;**7**:948

[87] M. Y. Shalaginov, V. V. Vorobyov, J. Liu, M. Ferrera, A. V. Akimov, A. Lagutchev, A. N. Smolyaninov, V. V. Klimov, J. Irudayaraj, A. V. Kildishev, A. Boltasseva, and V. M. Shalaev, Enhancement of single-photon emission from nitrogen-vacancy centers with TiN/(Al,Sc)N hyperbolic metamaterial, Laser & Photonics Reviews **9**, 120 (2015).

[88] Sakhdari M, Hajizadegan M, Farhat M, Chen P-Y. Efficient, broadband and wide-angle hot-electron

transduction using metal-semiconductor hyperbolic metamaterials. Nano Energy. 2016;**26**:371

[89] P.-Y. Chen, M. Hajizadegan, M. Sakhdari, and A. Alù, Giant Photoresponsivity of Midinfrared Hyperbolic Metamaterials in the Photon-Assisted-Tunneling Regime, Phys. Rev. Applied **5**, 041001 (2016).

[90] T. Guo, L. Zhu, P.-Y. Chen, and C. Argyropoulos, Tunable terahertz amplification based on photoexcited active graphene hyperbolic metamaterials [Invited], Opt. Mater. Express, OME **8**, 3941 (2018).

[91] M. Hajizadegan, M. Sakhdari, and P.-Y. Chen, in Micro- and Nanotechnology Sensors, Systems, and Applications X (International Society for Optics and Photonics, 2018), p. 106390M.

[92] N. Marcuvitz and M. I. of T. R. Laboratory, Waveguide Handbook (IET, 1951).

[93] Rozanov KN. Ultimate thickness to bandwidth ratio of radar absorbers. IEEE Transactions on Antennas and Propagation. 2000;**48**:1230

[94] Yin X, Long C, Li J, Zhu H, Chen L, Guan J, et al. Ultra-wideband microwave absorber by connecting multiple absorption bands of two different-sized hyperbolic metamaterial waveguide arrays. Scientific Reports. 2015;**5**:15367

[95] E. F. Knott, J. F. Schaeffer, and M. T. Tulley, Radar Cross Section (SciTech Publishing, 2004).

[96] Watts CM, Liu X, Padilla WJ. Metamaterial Electromagnetic Wave Absorbers. Advanced Materials. 2012; **24**:OP98

[97] Amin M, Siddiqui O, Farhat M, Khelif A. A perfect Fresnel acoustic reflector implemented by a Fano-resonant metascreen. Journal of Applied Physics. 2018;**123**:144502

[98] M. Amin, O. Siddiqui, and M. Farhat, Polarization-State Modulation in Fano Resonant Graphene Metasurface Reflector, Journal of Lightwave Technology 1 (2021).

[99] Ouyang L, Wang W, Rosenmann D, Czaplewski DA, Gao J, Yang X. Near-infrared chiral plasmonic metasurface absorbers. Opt. Express. 2018;**26**:31484

[100] M. Amin, O. Siddiqui, W. Orfali, M. Farhat, and A. Khelif, Resonant Beam Steering and Carpet Cloaking Using an Acoustic Transformational Metascreen, Phys. Rev. Applied **10**, 064030 (2018).

[101] Martini E, Mencagli M, Maci S. Metasurface transformation for surface wave control, Philosophical Transactions of the Royal Society A: Mathematical. Physical and Engineering Sciences. 2015;**373**:20140355

[102] Chen P-Y, Soric J, Padooru YR, Bernety HM, Yakovlev AB, Alù A. Nanostructured graphene metasurface for tunable terahertz cloaking, New J. Phys. 2013;**15**:123029

[103] L. Hsu, T. Lepetit, and B. Kanté, Extremely Thin Dielectric Metasurface for Carpet Cloaking, ArXiv:1503.08486 [Physics] (2015).

[104] Buchnev O, Podoliak N, Kaczmarek M, Zheludev NI, Fedotov VA. Electrically Controlled Nanostructured Metasurface Loaded with Liquid Crystal: Toward Multifunctional Photonic Switch. Advanced Optical Materials. 2015;**3**:674

[105] Komar A, Paniagua-Domínguez R, Miroshnichenko A, Yu YF, Kivshar YS, Kuznetsov AI, et al. Dynamic Beam Switching by Liquid Crystal Tunable Dielectric Metasurfaces. ACS Photonics. 2018;**5**:1742

[106] Artiga X, Bresciani D, Legay H, Perruisseau-Carrier J. Polarimetric Control of Reflective Metasurfaces. IEEE Antennas and Wireless Propagation Letters. 2012;**11**:1489

[107] Wu X, Meng Y, Wang L, Tian J, Dai S, Wen W. Anisotropic metasurface with near-unity circular polarization conversion. Appl. Phys. Lett. 2016;**108**: 183502

[108] Zhu HL, Cheung SW, Chung KL, Yuk TI. Linear-to-Circular Polarization Conversion Using Metasurface. IEEE Transactions on Antennas and Propagation. 2013;**61**:4615

[109] Koschny T, Kafesaki M, Economou EN, Soukoulis CM. Effective Medium Theory of Left-Handed Materials. Phys. Rev. Lett. 2004;**93**: 107402

[110] R. Liu, T. J. Cui, D. Huang, B. Zhao, and D. R. Smith, Description and explanation of electromagnetic behaviors in artificial metamaterials based on effective medium theory, Phys. Rev. E **76**, 026606 (2007).

[111] C. R. Simovski, On electromagnetic characterization and homogenization of nanostructured metamaterials, J. Opt. **13**, 013001 (2010).

[112] M. A. El-Aasser, Design optimization of nanostrip metamaterial perfect absorbers, JNP **8**, 083085 (2014).

[113] Hedayati MK, Javaherirahim M, Mozooni B, Abdelaziz R, Tavassolizadeh A, Chakravadhanula VSK, et al. Design of a Perfect Black Absorber at Visible Frequencies Using Plasmonic Metamaterials. Advanced Materials. 2011; **23**:5410

[114] Liu D, Wang L, Cui Q, Guo LJ. Planar Metasurfaces Enable High-Efficiency Colored Perovskite Solar Cells. Advanced Science. 2018;**5**:1800836

[115] D. B. Durham, S. R. Loria, F. Riminucci, K. Kanellopulos, X. Shen, F. Ciabattini, A. Mostacci, P. Musumeci, A. M. Minor, S. Cabrini, and D. Filippetto, in Plasmonics: Design, Materials, Fabrication, Characterization, and Applications XVIII (International Society for Optics and Photonics, 2020), p. 1146222.

[116] Locatelli A, Capobianco A-D, Midrio M, Boscolo S, De Angelis C. Graphene-assisted control of coupling between optical waveguides. Opt. Express. 2012;**20**:28479

[117] Farhat M, Rockstuhl C, Bağcı H. A 3D tunable and multi-frequency graphene plasmonic cloak, Opt. Express, OE. 2013;**21**(12592)

[118] Filter R, Farhat M, Steglich M, Alaee R, Rockstuhl C, Lederer F. Tunable graphene antennas for selective enhancement of THz-emission, Opt. Express, OE. 2013;**21**(3737)

[119] A. Vakil and N. Engheta, Fourier optics on graphene, Phys. Rev. B **85**, 075434 (2012).

[120] Gan X, Mak KF, Gao Y, You Y, Hatami F, Hone J, et al. Strong Enhancement of Light–Matter Interaction in Graphene Coupled to a Photonic Crystal Nanocavity. Nano Lett. 2012;**12**:5626

[121] Amin M, Farhat M, Bağcı H. A dynamically reconfigurable Fano metamaterial through graphene tuning for switching and sensing applications. Scientific Reports. 2013;**3**:2105